Title

Evolution of superconductivity in K2−xFe4+ySe5: Spectroscopic studies of X-ray absorption and emission

Journal

Proceedings of the National Academy of Sciences of the United States of America, 116(45)

ISSN

0027-8424

Authors

Wang, HT
Ghosh, Anirudha
Wang, CH
et al.

Publication Date

2019-11-05

DOI

10.1073/pnas.1912610116

Peer reviewed

Evolution of Superconductivity in $K_{2-x}Fe_{4+y}Se_5$: Spectroscopic Studies of X-ray Absorption and Emission

H. T. Wang[a,1], Anirudha Ghosh[b,1], C. H. Wang[c,d], S. H. Hsieh[b,e], Y. C. Shao[b,f], J. W. Chiou[g], C. L. Chen[e], C. W. Pao[e], J. F. Lee[e], Y. S. Liu[f], Y. D. Chuang[f], J. H. Guo[f], M. K. Wu[a,c,2] and W. F. Pong[b,2]

[a]Department of Physics, National Tsing Hua University, Hsinchu 30013, Taiwan; [b]Department of Physics, Tamkang University, Tamsui 25137, Taiwan; [c]Institute of Physics, Academia Sinica, Taipei 11529, Taiwan; [d]Department of Electronic and Computer Engineering, National University of Science and Technology, Taipei 10607, Taiwan; [e]National Synchrotron Radiation Research Center, Hsinchu 30076, Taiwan; [f]Advanced Light Source, Lawrence Berkeley National Laboratory, Berkeley, CA 94720, USA; [g]Department of Applied Physics, National University of Kaohsiung, Kaohsiung 81148, Taiwan

This study investigates the evolution of superconductivity in $K_{2-x}Fe_{4+y}Se_5$ using temperature-dependent X-ray absorption and resonant inelastic X-ray scattering techniques. Magnetization measurements show that polycrystalline superconducting (SC) $K_{1.9}Fe_{4.2}Se_5$ has a critical temperature (T_c) of ~31 K with a varying superconducting volume fraction, which strongly depends on its synthesis temperature. An increase in Fe-vacancy disorder in SC samples with more Fe-atoms occupying vacant 4**d** sites is found to be closely related to the decrease in the spin magnetic moment of Fe. Moreover, the nearest neighbor Fe–Se bond length in SC samples exceeds that in the non-SC (NS) sample, $K_2Fe_4Se_5$, which indicates a weaker hybridization between the Fe 3*d* and Se 4*p* states in SC samples. These results clearly demonstrate the correlations among the local electronic and atomic structures and the magnetic properties of $K_{2-x}Fe_{4+y}Se_5$ superconductors, providing deeper insight into the electron pairing mechanisms of superconductivity.

[1] H. T. Wang and Anirudha Ghosh contributed equally to this work

[2] To whom correspondence may be addressed. Email: mkwu@phys.sinica.edu.tw and wfpong@mail.tku.edu.tw.

Keyword: Superconductivity, Fe vacancy disorder, X-ray absorption spectroscopy, Resonant inelastic X-ray scattering

Introduction

Since the discovery of Fe-based superconductors (Fe-SCs) in 2008 (1), significant efforts have been made to better understand these materials. In particular, Fe-chalcogenide superconductors have attracted significant attention owing to a variety of characteristics, including a wide-range of critical temperatures (T_c), competition among various orders, and potential for the realization of Majorana bound state (2–10). The discovery of the alkali-intercalated iron selenide superconductor $A_{2-x}Fe_{4+y}Se_5$, where A = K, Rb and Cs, with a T_c of ~31 K (3, 11, 12) provided an opportunity for better understanding the origin of superconductivity in the Fe-chalcogenide family.

Several studies (12–17) have exploited various experimental techniques to explore the properties of $K_{2-x}Fe_{4+y}Se_5$, where x = 0–0.3 and y = 0.15–0.5. The parent compound, $K_2Fe_4Se_5$, forms a relatively complex antiferromagnetic (AFM, $T_N \approx$ 560 K) phase, where all Fe spin moments are oriented along the ***c***-axis at 16**i** sites. The crystal structure of $K_2Fe_4Se_5$ typically contains two Fe sites, 16**i** and 4**d**. Fe atoms occupy the 16**i** sites, whereas the 4**d** sites remain vacant, as shown in Fig. 1*A* (18). With an increase in the concentration of Fe atoms at the vacant 4**d** sites, a structural/vacancy-disordered superconducting material, $K_{2-x}Fe_{4+y}Se_5$, is formed with $T_c \approx$ 31 K. The most recent high-resolution temperature-dependent X-ray diffraction (XRD) analysis performed by Wang et al. (19), confirmed that the crystal lattice of superconducting $K_{2-x}Fe_{4+y}Se_5$ material exhibits the ***I4/m*** structural symmetry even at temperatures below the above mentioned T_c.

Detailed structural studies conducted by Wang et al. (19), verified that the emergence of superconductivity in $K_{2-x}Fe_{4+y}Se_5$ is not due to the impurity phase ($K_{0.5}Fe_2Se_2$), but due to the random occupation of Fe atoms in the lattice. However, several questions remain to be answered regarding the exact origin of the superconductivity. To gain deeper insight into the origin of superconductivity in this intriguing material, additional information is needed about its local electronic and atomic structure and magnetic properties (20–22). This study presents detailed experimental results of the temperature-dependent resonant inelastic X-ray scattering

(RIXS), X-ray absorption near-edge structure (XANES), and extended X-ray absorption fine structure (EXAFS) of powdered (SC) $K_{1.9}Fe_{4.2}Se_5$ and (NS) $K_2Fe_4Se_5$ samples. The obtained results elucidate the evolution of superconductivity and its association with the Fe-vacancy order–disorder, magnetic spin moments and Fe 3*d*-Se 4*p* hybridization in the $K_{2-x}Fe_{4+y}Se_5$ superconductor.

Significance

We employed X-ray absorption (XAS) and RIXS techniques to investigate the evolution of superconductivity in $K_{1.9}Fe_{4.2}Se_5$, which was synthesized from its NS parent compound, $K_2Fe_4Se_5$, by increasing the Fe concentration. $K_{1.9}Fe_{4.2}Se_5$ has $T_c \approx$ 31 K. The results provide a deeper insight into the magnetic and local electronic properties of $K_{1.9}Fe_{4.2}Se_5$, such as a decrease in AFM spin magnetic moment of Fe, charge transfer (CT) and hybridization between Fe 3*d*-Se 4*p* orbitals, and increase in the local static structural disorder, to gain an understanding of the evolution of superconductivity in the compound.

Results and Discussion

Polycrystalline SC $K_{1.9}Fe_{4.2}Se_5$ and NS $K_2Fe_4Se_5$ samples were synthesized by quenching at 820°C (SC-820 and NS-820) and 750°C (SC-750 and NS-750). Details regarding the sample preparation processes have been provided in two previous studies (16, 19). The crystal structure of the parent compound, $K_2Fe_4Se_5$ (phase group ***I4/m***), comprised a layer of K-atoms sandwiched between two Se–Fe–Se triple layer composites. The atoms comprising the triple layer are interconnected by $FeSe_4$ tetrahedra, as shown in Fig. 1*A*. Fe vacancies were identified at the Fe(4**d**) sites (12, 23). As the concentration of Fe in $K_{1.9}Fe_{4.2}Se_5$ is increased, the added Fe atoms primarily occupy the vacant 4**d** sites of the parent $K_2Fe_4Se_5$ compound. Figure 1*B* shows the room-temperature XRD patterns of all SC and NS samples. The overall ***I4/m*** crystal symmetry is conserved in both SC and NS samples with only a slight difference in their lattice parameters (19). Consequently, the XRD features are similar across the samples with an exception of the (002) peak intensity, which increases with respect to the intensity of the (123) peak in the SC samples. The XRD patterns [Fig. 1*B*] of all SC and NS samples reveal no additional second phase, detectable within the instrument resolution, in agreement with the report by Wang et al. (19). Figure 1*C* displays the

temperature-dependent magnetic susceptibility of all SC and NS samples in the temperature range 2–300 K, with the inset showing the susceptibility curve of the SC-750 sample near transition T_c= ~31 K. Although both SC-820 and SC-750 samples exhibit the same T_c, the diamagnetic signal of SC-820 is much larger than that of SC-750 (16).

Figure 2*A* displays the Fe $L_{\alpha,\beta}$ RIXS spectra of all SC and NS samples at 300 K. These were obtained at various excitation energies, labeled as **a**–**j** (green bars). The Fe $L_{3,2}$-edge XANES of the SC-820 sample at 300 K is shown in the inset of Fig. 2*A*. The RIXS spectrum denoted by **j,** with an excitation energy of 736.4 eV, shows two main emission features around 704.3 (L_α) and 717.4 eV (L_β), which occur due to the transition of electrons from the occupied Fe 3*d* states to the $2p_{3/2}$ and $2p_{1/2}$ core hole states (21, 24), respectively. The emission intensity of the $2p_{1/2}$ feature is weaker than the Fe L_2-edge XANES partially because of the Coster–Kronig decay of electrons from the Fe $2p_{3/2}$ to the $2p_{1/2}$ energy level (24). At all excitation energies from 707.0 to 736.4 eV, the RIXS spectra reveal a main feature around 704.3 eV (blue dashed line), resulting from the fluorescent feature whose position is independent of the excitation energy (20, 24). The low energy tail region of L_α is lower for SC samples in comparison with NS samples. This could imply a lower CT in SC samples than that in NS samples. In addition, an apparent shoulder-like feature (near 705.9 eV) is observed in the spectra **b**–**e** (close to the Fe L_3-edge excitation energy), which is a unique feature present only in $K_{2-x}Fe_{4+y}Se_5$ systems, whereas it is absent in other Fe-related superconductors (20, 24). For a better view of this shoulder-like feature, the energy-loss RIXS spectra, **d**, of all samples are plotted in Fig. 2*B*. An Fe metal sample is used as a reference.

The spectral feature at the zero energy loss of the Fe metal in Fig. 2*B* arises from elastic scattering. Since all RIXS spectra for Fe metal, SC, and NS samples were collected at the same scattering angle, the absence of the elastic feature in SC and NS samples may be due to their higher surface roughness and density of defects compared to those of the Fe metal. The fluorescent feature near ~−3.5 eV (blue dashed line) is observed in all samples and Fe metal, which is due to the emission from Fe 3*d* to $2p_{3/2}$ (L_α). The shoulder-like feature near −1.9 eV in Fig. 2*B* arises from the intra-electronic transition from Fe t_{2g} to e_g states and is referred to as the *d*–*d* excitation (21, 25, 26). The *d*–*d* excitation feature is prominent in the **b–e** spectra, whereas it is embedded in the high energy tail of the **f** spectra and appears as humps (black arrows) in **g** and **h**. In

the spectra of **a** and **i**, it possibly lies hidden within the L_α and L_β peaks. The emergence of this *d–d* excitation feature −1.9 eV, Fig. 2*B*, in both SC and NS samples suggests considerable crystal field splitting of Fe ions in the $FeSe_4$ tetrahedra.

Figure 2*C* shows the Fe $L_{\alpha,\beta}$ RIXS spectra of **i** (720.4 eV) of SC and NS samples at 300 and 20 K. Two prominent emission features, L_α and L_β, are observed for all samples. We calculate the resonant ratio (RR) of the integrated intensities, I_β/I_α (I_β: 695.0–710.0 eV and I_α: 710.0–725.0 eV in the emission spectrum), to provide insight into the local spin states of Fe ions in SC and NS samples at both 300 and 20 K. The RRs of all samples, as shown in the inset in Fig. 2*C*, are closely related to the variation of the samples' magnetic spin state (22, 27). A higher value of RR typically reflects a higher magnetic moment of magnetic ions. As shown in the inset in Fig. 2*C*, the RRs of SC and NS samples at both temperatures lie between the corresponding values for FeO (1.38) and Fe metal (0.40), implying an intermediate spin magnetic moment of Fe ions. A comparison of the RRs of the SC samples with those of the NS samples reveals that not only they decrease with higher Fe concentration but also decrease with the higher quenching temperature. This decrease in the magnetic moment of Fe ions in the SC samples may arise from the magnetic frustration of Fe spins in the material which is caused by the occupation of additional Fe ions at the vacant 4**d** sites (28). This significant decrease in the antiferromagnetic (AFM) moment in SC samples is in agreement with another report (29) and may not responsible for the electron pairing mechanism in the evolution of superconductivity (30, 31).

To obtain a deeper insight into the evolution of superconductivity, we investigated the CT/hybridization property of both SC and NS samples (32, 33). Accordingly, we acquired the Fe $L_{3,2}$-edge and Se *K*-edge XANES spectra of the samples, which provide valuable information to investigate the electronic structures at/near the Fermi level (34–36). Figure 3*A* presents the Fe $L_{3,2}$-edge XANES of SC and NS samples measured at 300 and 20 K. The L_3- (~707.8 eV) and L_2- (~720.8 eV) edge features of the Fe $L_{3,2}$-edge XANES are dominated by electron transitions from the Fe $2p_{3/2}$ and $2p_{1/2}$ to unoccupied 3*d* states above the Fermi level, respectively. All spectra are normalized at the pre L_3 and post L_2- edges region. The general line shape of the spectra of SC and NS samples in Fig. 3*A* is consistent with that of other Fe-chalcogenide superconductors (20, 22). The insets (top and bottom at 300 and 20 K, respectively) in Fig. 3*A* indicate that the intensity of the white-line feature at the Fe L_3-edge XANES of SC samples is

lower than that of the NS samples at both temperatures. The intensity of the white-line of the SC-820 (NS-750) sample is the lowest (highest) at both temperatures. These results indicate that the Fe 3*d* energy levels in SC samples have fewer unoccupied (hole) states compared to NS samples.

To better understand the difference in the CT between Fe 3*d* and Se 4*p* states, Se *K*-edge XANES measurements of SC and NS samples were conducted at 300 K; the results are shown in Fig. 3*B*. The general line shape of the XANES spectra clearly exhibit three prominent features depicted by **A**–**C**. Feature **A** designates the electron excitation from Se 1*s* to the unoccupied Se 4*p* states above the Fermi level, whereas the other two features **B** and **C** arise from the scattering of emitted photoelectrons by the nearest neighbor (NN) and next NN of Fe and Se atoms (37). Here we refer CT as this variation in the electron occupancies in Fe 3*d* and Se 4*p* orbitals which primarily occur due to change in Fe 3*d*-Se 4*p* covalent mixing in SC and NS samples. The top inset in Fig. 3*B* illustrates the magnified details of feature **A**. The intensity of feature **A** increases from NS (NS-750→NS-820) to SC (SC-750→SC-820) samples, on the contrary to the trend exhibited by the white-line intensity at the Fe L_3-edge absorption for NS and SC samples, as shown in the insets of Fig. 3*A*. For a better analysis of the CT phenomenon between Fe 3*d* and Se 4*p* states, the corresponding background is subtracted from their respective spectrum. The integrated intensities of the white-line in the Fe L_3-edge absorption spectra (between 704.0 and 717.6 eV) at 300 and 20 K and the feature **A** in the Se *K*-edge XANES spectra (between 12,654.4 and 12,660.4 eV) at 300 K are obtained, as shown in the lower inset of Fig. 3*B*. These results clearly indicate a lower CT between Fe 3*d* and Se 4*p* states in SC samples than in NS samples, which is in agreement with our RIXS analysis (Fig. 2*A*). The CT-type Mott insulating property of the NS sample has been proposed in a previous study (32), which suggests a strong CT in the material. The decrease in CT/hybridization between Fe 3*d*-Se 4*p* states in SC samples lead to the reduction of Fe 3*d* un-occupancy (hole), and therefore explains the orbital-selective disappearance of spectral weight in one of the Fe 3*d* orbitals. This observation is in agreement with the orbital-selective Mott phase (30, 31), which suggests that the pairing mechanism in superconductivity may arise from local electron exchange interactions. Therefore, the present results implying the electron–electron correlation is mediated by the local electron exchange interactions, without the involvement of Fe spins, in the evolution to superconductivity in SC samples. However, we cannot rule out that the Fe spin fluctuations, associated with the decrease in Fe magnetic moment in SC samples based on the RIXS results, can be the source to mediate the electron-electron pairing mechanism in the evolution to superconductivity.

In our earlier discussion on the Fe $L_{\alpha,\beta}$ RIXS spectra, we showed that the variations in the magnetic moment of SC and NS samples are closely associated with the

occupation of Fe-vacant sites, which is consistent with the results of detailed structural studies provided by Wang et al. (19). To further understand this observation, we have conducted element-specific EXAFS measurements at the Fe *K*-edge. Figure 4*A* displays the Fe *K*-edge Fourier transform (FT) spectra of SC and NS samples at 300 and 20 K, and the inset shows the corresponding EXAFS oscillations. The FT spectra exhibit only one feature because of experimental uncertainty and the small difference in bond lengths of NN Fe-Se and Fe-Fe bond (~2.4 and 2.7 Å, respectively). (37). The quantitative details of the short range local environment of Fe atoms in SC and NS samples, such as the coordination number (CN), bond length (R), and Debye–Waller factor [DWF, $\sigma^2(T)$], are obtained from the Fe *K*-edge EXAFS spectra at both 300 and 20 K using the Arthemis fitting program (38, 39), and the results are shown in Figs. 4*B–D*, respectively. As shown in Fig. 4*B*, the $CN_{Fe–Fe}$, which is related to the Fe concentration, is substantially higher for SC samples than for NS samples at both temperatures (SC-820 has the highest $CN_{Fe–Fe}$). Earlier studies (16, 18, 19) have shown that the Fe(4**d**) sites in the parent compound, $K_2Fe_4Se_5$, are vacant, such that additional Fe ions preferentially occupy the vacant 4**d** sites. Therefore, an increase in the Fe concentration at the vacant 4**d** sites in SC samples (particularly in the SC-820 sample) will increase the overall $CN_{Fe–Fe}$ around the Fe sites. Furthermore, the CN Fe–Fe of SC-820 sample is higher than that of the SC-750 sample at both 300 and 20 K, which is consistent with the result of higher occupation of Fe(4d) sites reported (19). On the contrary, the NS (NS-820 and NS-750) samples exhibit no significant change in $CN_{Fe–Fe}$, which is expected, as no additional Fe atoms are presented to occupy the vacant 4**d** sites. This result demonstrates that the SC-820 sample comprises more Fe atoms that occupy the vacant 4**d** sites, which can contribute to structural/vacancy disorder in the material (16, 19). The data exhibit no significant difference in $CN_{Fe–Se}$ values between SC and NS samples, which reveals an unaltered $FeSe_4$ tetrahedral network in both samples, consistently with the discussion in Fig. 2*B*. Figure 4*C* shows a significant increase in both the Fe–Se and Fe–Fe bond lengths of SC samples compared to the NS samples. This finding is consistent with the increase in occupation of vacant Fe(4**d**) sites in SC samples (19). The larger bond length is likewise consistent with the decrease in Fe 3*d*-Se 4*p* hybridization and CT between Fe 3*d* and Se 4*p* states in the SC samples as than in the NS samples.

Figure 4*D* presents the variation in the DWF derived from the NN Fe–Se and Fe–

Fe bonds at 300 and 20 K. The DWFs of Fe–Se and Fe–Fe bonds in SC samples are much higher than those in the NS samples. The DWF that derives from the Fe–Fe bonds in SC-820 is higher than that of SC-750 at both temperatures, whereas there is no significant variation in the DWF related to Fe–Se or Fe–Fe bonds in NS-820 and NS-750 samples. This finding strongly indicates that the SC samples, particularly SC-820, which has the highest SC volume fraction, have greater local structural disorder around the Fe atoms than the NS samples at both measured temperatures. Furthermore, a close examination of Fig. 4*D* reveals no significant variation in the DWF corresponding to Fe–Se bonds between SC-820 and SC-750 samples at either temperature.

To gain a comprehensive understanding of the temperature-dependent local atomic structures that correspond to the NN Fe–Se and Fe–Fe bonds in the SC and NS samples, Figs. 5*A* and *B* plot the temperature-dependent FT of the Fe *K*-edge EXAFS spectra of SC-750 and NS-750 samples, respectively, from 300 to 20 K. The insets show the corresponding $k^2\chi$ oscillations. Figure 5*C* displays the temperature-dependent NN Fe–Se and Fe–Fe bond lengths that are obtained from the fitted EXAFS spectra. The Fe–Se and Fe–Fe bond lengths in both samples in the range of 20–300 K are fairly temperature-independent, revealing no structural transition in the measured range, which is in agreement with the neutron diffraction investigation (12). Both Fe–Se and Fe–Fe bond lengths are higher in SC samples than in NS samples in the measured temperature range. Figure 5*D* shows the plot of the DWF [σ^2(T)] for Fe–Se and Fe–Fe bond as a function of temperature. The DWF [σ^2(T)] generally comprises two components, σ^2_{stat} and $\sigma^2(T)_{vib}$, which are associated with the temperature-independent static atomic disorder and the temperature-dependent thermal vibrations (39), respectively. $\sigma^2(T)_{vib}$ generally become smaller as the temperature decreases. Therefore, with a decrease in the temperature, the σ^2(T) of the SC-750 and NS-750 samples also decreases due to $\sigma^2(T)_{vib}$ factor, as shown in Fig. 5*D*. The SC-750 sample has a higher DWF for both bond correlations in the entire measured temperature range. Notably, in the low temperature range (below 50 K), there is no significant temperature dependence. Therefore, we extrapolate this linear region to 0 K, where the thermal vibrations are absent and DWF's primary contribution is due to the σ^2_{stat} component. The DWF at 0 K reveals that the σ^2_{stat} values of the SC-750 sample are ~3.0×10^{-3} and ~1.9×10^{-3} Å^2 for Fe–Se and Fe–Fe bond correlations, respectively, which are significantly higher than the corresponding bond correlations (~1.1×10^{-3} and ~0.7×10^{-3} Å^2) of the NS-750

sample. As discussed above, the static disorder component arises from the local structural disorder; hence, the higher σ_{stat}^2 components of DWF reveal an increase in the structural/vacancy disorder with higher Fe concentration at the 4**d** sites in SC-750. In NS-750, however, vacant 4**d** sites are mostly ordered, and therefore the σ_{stat}^2 is significantly lower than that of SC-750. Detailed theoretical calculations, based on the variation in the DWF, should certainly provide a perspective in future studies to understand whether any electron-phonon coupling co-exists in the present system along with electron-electron correlation.

Conclusion

In summary, temperature-dependent XANES and EXAFS measurements both provide evidence of the Fe 3*d* and Se 4*p* hybridized states and a strong static disorder of Fe atoms, elucidating the evolution of superconductivity of SC ($K_{1.9}Fe_{4.2}Se_5$) samples. The magnetic and EXAFS data analyses reveal that the superconducting volume fraction can be enhanced by quenching at a higher temperature during the sample synthesis procedure, thereby increasing the structural/vacancy disorder around Fe atoms, as depicted in the SC-820 sample. An analysis of the RR based on RIXS spectra reveals a decrease in the magnetic moment of Fe ions resulting from the occupation of Fe at the vacant 4**d** sites, and thereby reducing the overall magnetic moment in SC samples. Furthermore, an increase in the Fe–Se bond length in SC samples reflects a reduction in hybridization and CT between Fe 3*d* and Se 4*p* states. These results support electron-electron pairing mechanism, mediated by local electron exchange interaction, in the evolution of superconductivity in $K_{1.9}Fe_{4.2}Se_5$. Finally, we believe that the results present here provide the detailed element selective local electronic/atomic information, which certainly are valuable to better understand the origin of superconductivity in Fe-chalcogenide superconductors.

Methods

Preparation and Characterization of Samples

Polycrystalline superconducting $K_{1.9}Fe_{4.2}Se_5$ (SC) and non-superconducting $K_2Fe_4Se_5$ (NS) samples were synthesized by quenching these compounds at 820 °C (SC-820 and NS-820) and 750 °C (SC-750 and NS-750). The detailed procedure is provided in previous studies (16, 19). Room-temperature XRD experiments were conducted with an in-house X-ray diffractometer with Cu $K_{\alpha 1}$ radiation to characterize the crystalline structures of the SC and NS samples. To investigate the interplay of various parameters that drive the evolution of superconductivity, temperature-dependent magnetic susceptibility, RIXS, XANES, and EXAFS experiments were carried out. Magnetic susceptibility measurements were performed using a superconducting quantum interference device. The Fe $L_{3,2}$-edge XANES and Fe $L_{\alpha,\beta}$ RIXS were measured at the *i*RIXS-endstation (40), at beamline 8.0.1 of the Advanced Light Source at Lawrence Berkeley National Laboratory, Berkeley, USA. The Se *K*-edge XANES and Fe *K*-edge EXAFS spectra were obtained in bulk sensitive total fluorescence yield mode at the SWLS-01C and Wiggler-17C beamlines, respectively, at the Taiwan Light Source of National Synchrotron Radiation Research Center, Taiwan. The energy resolutions of the XANES measurements were set to ~0.1 eV at the Fe $L_{3,2}$-edge and ~0.5/1.0 eV at the Fe/Se *K*-edge, respectively. Fe and Se foils were used to calibrate the photon energy at the corresponding edges.

Figure Captions

Figure 1. (*A*) Unit cell of crystal structure of $K_2Fe_4Se_5$ with ***I4/m*** space group. The crystal structure is comprised of alternating layers of alkali, K, atoms, and interconnected $FeSe_4$ tetrahedra. The Se–Fe–Se layer contains two sets of Fe sites: Fe(16**i**) are 16**i** sites that are occupied by Fe atoms (right-bottom), whereas Fe(4**d**) are vacant 4**d** sites (left-bottom). (*B*) Room-temperature XRD patterns of all samples, revealing similar majority ***I4/m*** phase. (*C*) Temperature-dependent magnetic susceptibility reveals a superconducting transition temperature of T_c~ 31 K in SC samples. The inset magnifies the temperature-dependent magnetic susceptibility plot of SC-750.

Figure 2. (*A*) Fe $L_{\alpha,\beta}$ RIXS spectra of SC and NS samples obtained at various excitation energies (**a**–**j**), which are indicated by Fe $L_{3,2}$-edge XANES (shown in upper inset). Two main features, L_α (~704.3 eV) and L_β (~717.4 eV), arise from transitions from 3*d* to $2p_{3/2}$ and $2p_{1/2}$ states, respectively. Small bump-like features originate from the *d*-*d* excitation, are indicated by the downward arrows. (*B*) Energy-loss feature of Fe $L_{\alpha,\beta}$ RIXS with resonant excitation energy of 707.8 eV in SC and NS samples. The black solid line at 0 eV represents the elastic peak of reference Fe metal, while the red (blue) dashed line at an energy loss of approximately –1.9 eV (–3.5 eV) corresponds to Fe *d*-*d* excitation (fluorescence) feature. (*C*) Fe $L_{\alpha,\beta}$ RIXS spectra of SC and NS samples at an excitation energy of 720.4 eV (corresponding to L_2-edge) at 300 K and 20K. The inset plots the variation of RRs (I_β/I_α) of SC and NS samples at 300 K and 20 K.

Figure 3. (*A*) Fe $L_{3,2}$-edge XANES of SC and NS samples at 300 K and 20 K. Insets magnify the L_3-edge feature. Black dashed lines depict the best-fitted arctangent function, which are representative of the background intensity that arises from the transition to the continuum band above the Fermi level. (*B*) Se *K*-edge XANES spectra of SC and NS samples at 300 K. The upper inset magnifies the feature "**A**." The lower inset plots variation of integrated intensities of the white-line feature at the Fe L_3-edge and feature "**A**" at the Se *K*-edge of SC and NS samples. The tail of the **B** Gaussian feature is considered as the background and depicted by a black dashed line.

Figure 4. (*A*) Magnitude of Fe *K*-edge FT spectra of SC and NS samples at 300 K and

20 K. The inset displays the corresponding EXAFS data, $k^2\chi$, within the range k = 3.0–14.1 Å. The solid line depicts the fit obtained using Artemis programs, and open symbols represent results obtained from experimental data. Parameters obtained from fitting the FT spectra of SC and NS samples are (*B*) coordination numbers $CN_{Fe\text{-}Se}$ and $CN_{Fe–Fe}$ (*C*) Fe–Se and Fe–Fe bond lengths, R, and (*D*) Fe–Se and Fe–Fe DWF, σ^2(T), at 300 K and 20 K.

Figure 5. Temperature-dependent FT magnitudes of Fe *K*-edge EXAFS of (*A*) SC-750 (*B*) NS-750 samples. Insets show the corresponding EXAFS data, $k^2\chi$, within the range k = 3.0–14.1 Å. Parameters obtained from the fitted FT spectra are (*C*) NN Fe–Se and Fe–Fe bond lengths, R, and (*D*) DWF, σ^2(T), as a function of temperature for SC-750 and NS-750 samples. Green lines represent the extrapolation of the low temperature range, 75–20 K of DWF data, to 0 K.

References

1. Y. Kamihara, T. Watanabe, M. Hirano, H. Hosono, Iron-Based Layered Superconductor La($O_{1-x}F_x$)FeAs (x= 0.05-0.12) with Tc= 26 K. *J. Am. Chem. Soc.* **130**, 3296-3297 (2008).
2. M. K. Wu *et al.,* An overview of the Fe-chalcogenide superconductors. *J. Phys. D Appl. Phys.* **48**, 323001 (2015).
3. E. Dagotto, Colloquium: The unexpected properties of alkali metal iron selenide superconductors. *Rev. Mod. Phys.* **85**, 849-867 (2013).
4. F. C. Hsu *et al*., Superconductivity in the PbO-type structure α-FeSe. *Proc. Nat. Acad. Sci. U. S. A.* **105**, 14262-14264 (2008).
5. Q. Si, R. Yu, E. Abrahams, High-temperature superconductivity in iron pnictides and chalcogenides. *Nat. Rev. Mater.* **1**, 16017 (2016).
6. M. K. Wu *et al*., The development of the superconducting PbO-type β-FeSe and related compounds. *Physica C* **469**, 340-349 (2009).
7. Y. Mizuguchi *et al*., Anion height dependence of Tc for the Fe-based superconductor. *Supercond. Sci. Technol.* **23**, 054013 (2010).
8. M. H. Fang *et al.*, Superconductivity close to magnetic instability in $Fe(Se_{1-x}Te_x)_{0.82}$. *Phys. Rev. B* **78**, 224503 (2008).
9. P. Dai, Antiferromagnetic order and spin dynamics in iron-based superconductors. *Rev. Mod. Phys.* **87**, 855-891 (2015).
10. D. Wang *et al*., Evidence for Majorana bound states in an iron-based superconductor. *Science* **362,** 333-335 (2018).
11. J. Guo *et al.*, Superconductivity in the iron selenide $K_xFe_2Se_2$ ($0 \leq x \leq 1.0$). *Phys. Rev. B* **82**, 180520(R) (2010).
12. F. Ye *et al*., Common crystalline and magnetic structure of superconducting $A_2Fe_4Se_5$ (A= K, Rb, Cs, Tl) single crystals measured using neutron diffraction. *Phys. Rev. Lett.* **107,** 137003 (2011).
13. A. Ricci *et al.,* Direct observation of nanoscale interface phase in the superconducting chalcogenide $K_xFe_{2-y}Se_2$ with intrinsic phase separation. *Phys. Rev. B* **91,** 020503(R) (2015).
14. Z. Shermadini *et al.,* Superconducting properties of single-crystalline $A_xFe_{2-y}Se_2$ (A= Rb, K) studied using muon spin spectroscopy. *Phys. Rev. B* **85,** 100501(R) (2012).

15. Y. J. Yan *et al.,* Electronic and magnetic phase diagram in $K_xFe_{2-y}Se_2$ superconductors. *Sci. Rep.* **2,** 212 (2012).
16. C. H. Wang *et al.*, Disordered Fe vacancies and superconductivity in potassium-intercalated iron selenide ($K_{2-x}Fe_{4+y}Se_5$). *Europhys Lett* **111**, 27004 (2015).
17. Z. Wang *et al.,* Archimedean solidlike superconducting framework in phase-separated $K_{0.8}Fe_{1.6+x}Se_2$ ($0 \leq x \leq 0.15$). *Phys. Rev. B* **91**, 064513 (2015).
18. D. P. Shoemaker *et al.,* Phase relations in $K_xFe_{2-y}Se_2$ and the structure of superconducting $K_xFe_2Se_2$ via high-resolution synchrotron diffraction. *Phys. Rev. B* **86,** 184511 (2012).
19. C. H. Wang *et al.,* Role of the extra Fe in $K_{2-x}Fe_{4+y}Se_5$ superconductors. *Proc. Nat. Acad. Sci. U. S. A.* **116**, 1104-1109 (2019).
20. C. L. Chen *et al.,* X-ray spectra and electronic correlations of $FeSe_{1-x}Te_x$. *Phys. Chem. Chem. Phys.* **13,** 15666-15672 (2011).
21. L. J. P. Ament, M. van Veenendaal, T. P. Devereaux, J. P. Hill, J. van den Brink, Resonant inelastic X-ray scattering studies of elementary excitations. *Rev. Mod. Phys.* **83**, 705-767 (2011).
22. I. Perez *et al.,* Electronic structure of Co-substituted FeSe superconductor probed by soft X-ray spectroscopy and density functional theory. *Phys. Rev. B* **90,** 014510 (2014).
23. Y. J. Song *et al.,* Phase transition, superstructure and physical properties of $K_2Fe_4Se_5$. *Europhys Lett* **95,** 37007 (2011).
24. W. L. Yang *et al.,* Evidence for weak electronic correlations in iron pnictides. *Phys. Rev. B* **80,** 014508 (2009).
25. C. Monney *et al.,* Resonant inelastic x-ray scattering at the Fe L_3-edge of the one-dimensional chalcogenide $BaFe_2Se_3$. *Phys. Rev. B* **88,** 165103 (2013).
26. T. Nomura *et al.,* Resonant inelastic X-ray scattering study of entangled spin-orbital excitations in superconducting $PrFeAsO_{0.7}$. *Phys. Rev. B* **94,** 035134 (2016).
27. K. C. Prince *et al.,* Core-level spectroscopic study of FeO and FeS_2. *Phys. Rev. B* **71**, 085102 (2005).
28. Q. Si, E. Abrahams, Strong Correlations and Magnetic Frustration in the High T_c Iron Pnictides. *Phys. Rev. Lett.* **101,** 076401 (2008).

29. S. Li *et al.,* Suppression of the antiferromagnetic order when approaching the superconducting state in a phase-separated crystal of $K_xFe_{2-y}Se_2$. *Phys. Rev. B* **96,** 094503 (2017).
30. M. Yi *et al.,* Observation of universal strong orbital-dependent correlation effects in iron chalcogenides. *Nat. Commun.* **6**, 7777 (2015).
31. R. Yu, Q. Si, Orbital-Selective Mott Phase in Multiorbital Models for Alkaline Iron Selenides $K_{1-x}Fe_{2-y}Se_2$. *Phys. Rev. Lett.* **110**, 14640 (2013).
32. M. Oiwake *et al.,* Electronic structure and phase separation of superconducting and nonsuperconducting $K_xFe_{2-y}Se_2$ revealed by X-ray photoemission spectroscopy. *Phys. Rev. B* **88**, 224517 (2013).
33. C. Cao, F. Zhang, Electronic structure of vacancy-ordered iron-selenide $K_{0.5}Fe_{1.75}Se_2$. *Phys. Rev. B* **87,** 161105(R) (2013).
34. H. T. Wang *et al.,* Electronic and atomic structures of the $Sr_3Ir_4Sn_{13}$ single crystal: A possible charge density wave material. *Sci. Rep.* **7**, 40886 (2017).
35. S. H. Hsieh *et al.,* Anisotropy in the thermal hysteresis of resistivity and charge density wave nature of single crystal $SrFeO_{3-\delta}$: X-ray absorption and photoemission studies. *Sci. Rep.* **7,** 161 (2017).
36. A. Ghosh *et al.*, Anisotropy in the magnetic interaction and lattice-orbital coupling of single crystal Ni_3TeO_6. *Sci. Rep.* **8**, 15779 (2018).
37. A. Iadecola *et al.*, Local structure response of phase separation and iron-vacancy order in $K_xFe_{2-y}Se_2$ superconductor. *Phys. Rev. B* **90**, 174509 (2014).
38. J. J. Rehr, J. Mustre de Leon, S. I. Zabinsky, R. C. Albers, Theoretical X-ray absorption fine structure standards. *J. Am. Chem. Soc.* **113**, 5135-5140 (1991).
39. A. I. Frenkel, E. A. Stern, M. Qian, M. Newville, Multiple-scattering X-ray-absorption fine-structure analysis and thermal expansion of alkali halides. *Phys. Rev. B* **48**, 12449 (1993).
40. Y. D. Chuang *et al.*, Modular soft x-ray spectrometer for applications in energy sciences and quantum materials. *Rev. Sci. Instrum.* **88**, 013110 (2017).

Acknowledgements

The authors M. K. Wu and W.F.P. would like to thank the Ministry of Science and Technology (MoST) of Taiwan for providing financial support for the research under the projects MoST 106-2633M-001-001, 105-2112-M-032-001-MY3 and 106-2632-M-032-001-MY3. M. K. Wu also thanks Academia Sinica Thematic Research Grant AS-TP-106-M01.

Author Contributions

H.T.W., A.G, and W.F.P. designed the experiments after discussion with M.K.W. The SC and NS samples were synthesized by C.H.W. and M.K.W. All XAS and RIXS measurements were performed by H.T.W., A.G., S.H.H., Y.C.S., J.W.C., C.L.C., C.W.P., J.F.L., Y.S.L., Y.D.C. and J.H.G. The data analysis and writing of the manuscript were done by H.T.W, A.G., M.K.W and W.F.P. All authors discussed the results and contributed to the finalization of the manuscript.

Additional Information

Competing Interests: The authors declare no competing interests.

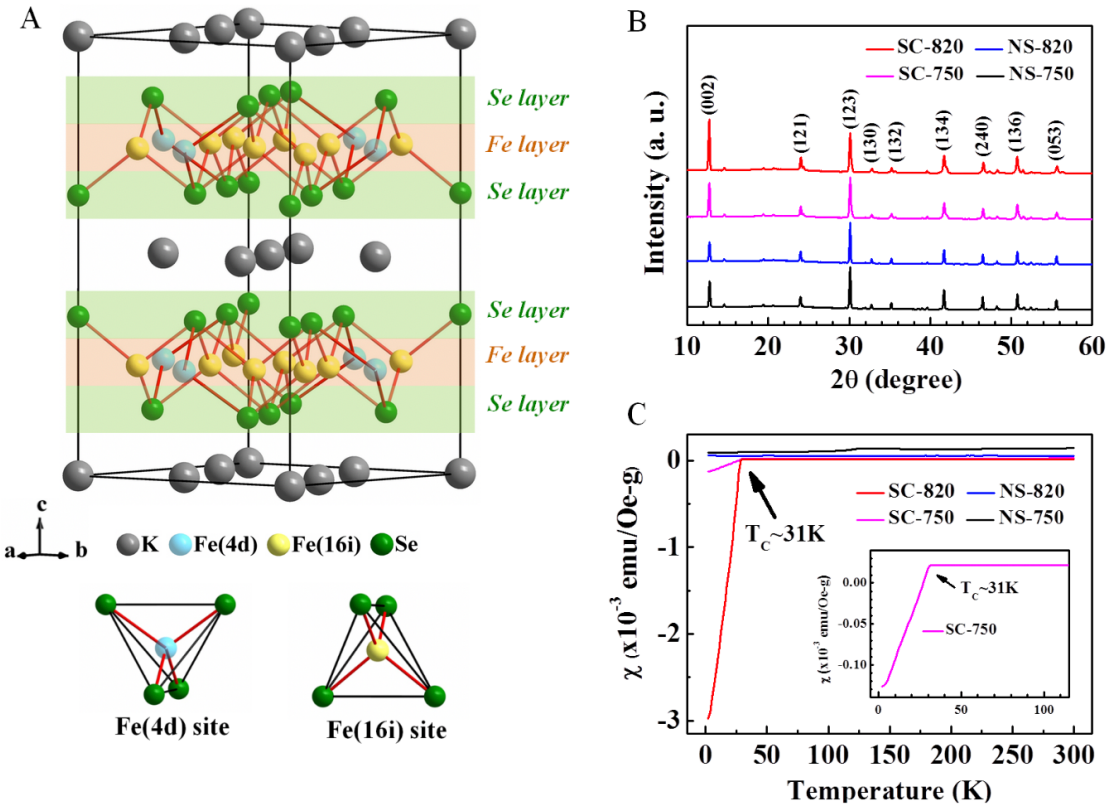
A
Se layer
Fe layer
Se layer
Se layer
Fe layer
Se layer
c
a
b
K
Fe(4d)
Fe(16i)
Se
Fe(4d) site
Fe(16i) site
B
SC-820
NS-820
SC-750
NS-750
(002)
(121)
(123)
(130)
(132)
(134)
(240)
(136)
(053)
Intensity (a. u.)
10
20
30
40
50
60
2θ (degree)
C
SC-820
NS-820
SC-750
NS-750
T_C~31K
χ (x10^-3 emu/Oe-g)
0
-1
-2
-3
0
50
100
150
200
250
300
Temperature (K)
T_C~31K
SC-750
0.00
-0.05
-0.10
0
50
100

Figure 1

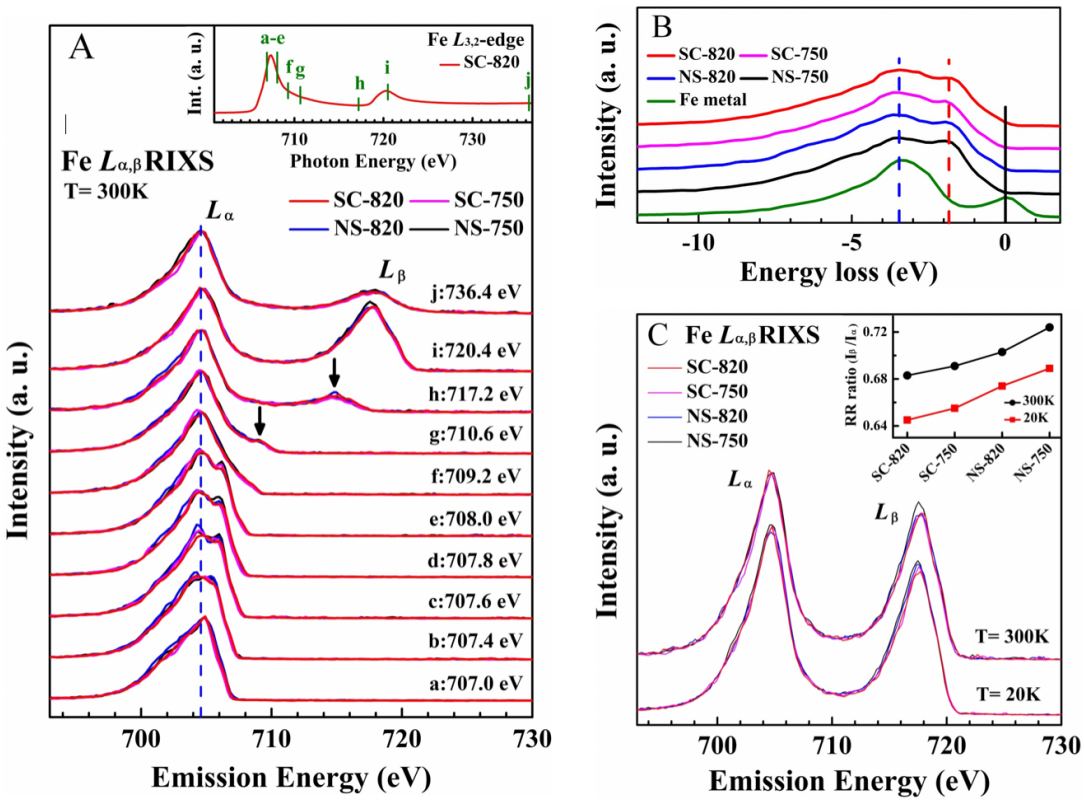
A
Fe $L_{3,2}$-edge
SC-820
a-e
f g
h
i
j
Int. (a. u.)
710
720
730
Photon Energy (eV)
Fe $L_{\alpha,\beta}$ RIXS
T= 300K
SC-820
SC-750
NS-820
NS-750
L_α
L_β
j:736.4 eV
i:720.4 eV
h:717.2 eV
g:710.6 eV
f:709.2 eV
e:708.0 eV
d:707.8 eV
c:707.6 eV
b:707.4 eV
a:707.0 eV
Intensity (a. u.)
700
710
720
730
Emission Energy (eV)
B
SC-820
SC-750
NS-820
NS-750
Fe metal
Intensity (a. u.)
-10
-5
0
Energy loss (eV)
C
Fe $L_{\alpha,\beta}$ RIXS
SC-820
SC-750
NS-820
NS-750
RR ratio (I_β /I_α)
0.72
0.68
0.64
300K
20K
SC-820
SC-750
NS-820
NS-750
L_α
L_β
T= 300K
T= 20K
Intensity (a. u.)
700
710
720
730
Emission Energy (eV)

Figure 2

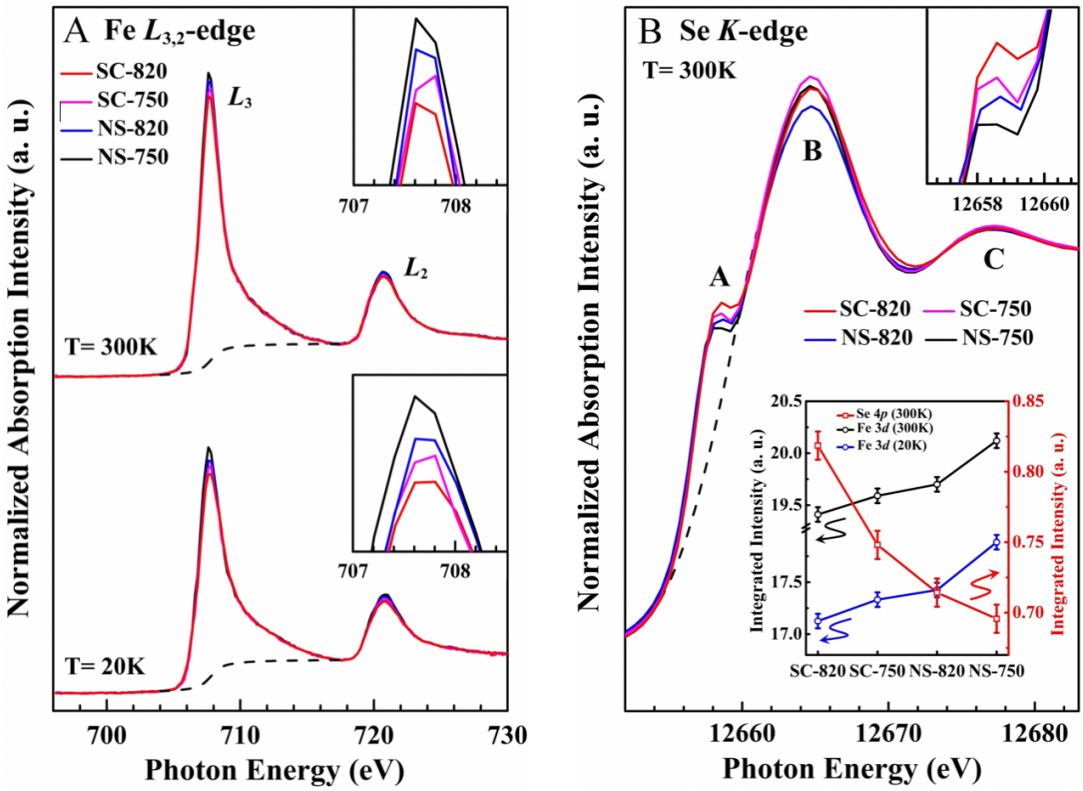
A Fe $L_{3,2}$-edge
SC-820
SC-750
NS-820
NS-750
L_3
L_2
T= 300K
T= 20K
707
708
Normalized Absorption Intensity (a. u.)
700
710
720
730
Photon Energy (eV)
B Se K-edge
T= 300K
A
B
C
12658
12660
SC-820
SC-750
NS-820
NS-750
Se 4p (300K)
Fe 3d (300K)
Fe 3d (20K)
Integrated Intensity (a. u.)
20.5
20.0
19.5
17.5
17.0
0.85
0.80
0.75
0.70
SC-820 SC-750 NS-820 NS-750
12660
12670
12680
Photon Energy (eV)

Figure 3

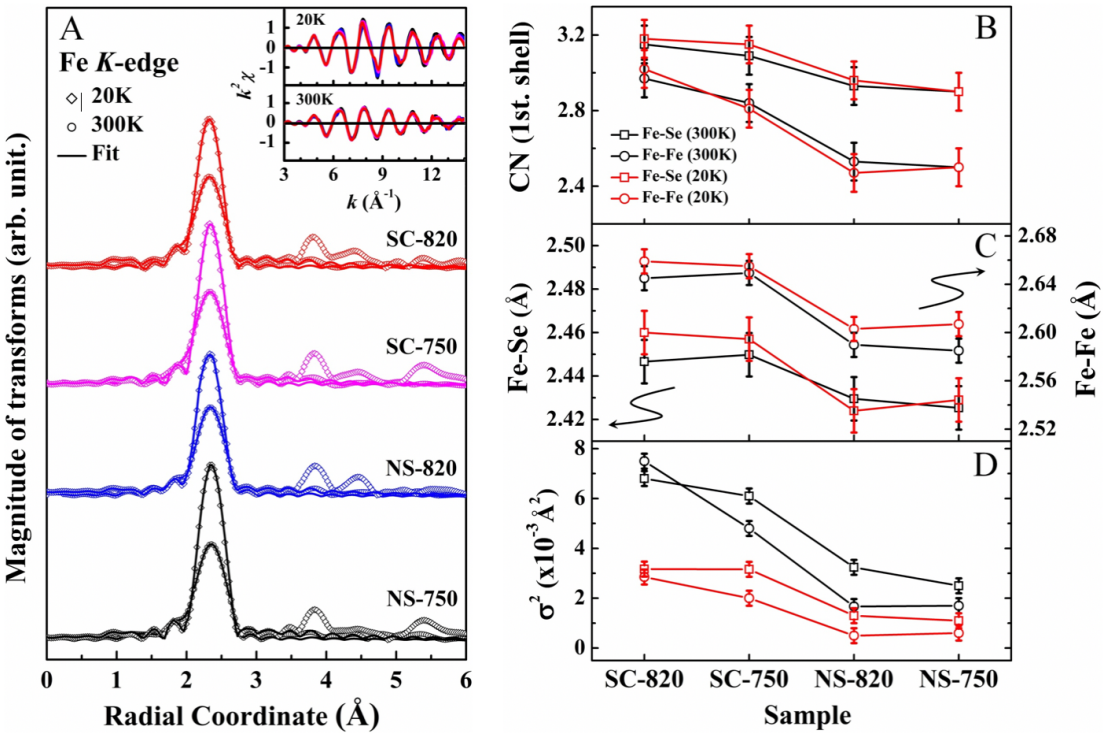
A
Fe K-edge
20K
300K
Fit
20K
300K
$k^2\chi$
k (Å^{-1})
SC-820
SC-750
NS-820
NS-750
Magnitude of transforms (arb. unit.)
Radial Coordinate (Å)
B
CN (1st. shell)
Fe-Se (300K)
Fe-Fe (300K)
Fe-Se (20K)
Fe-Fe (20K)
C
Fe-Se (Å)
Fe-Fe (Å)
D
σ^2 (x10^{-3} Å^2)
SC-820
SC-750
NS-820
NS-750
Sample

Figure 4

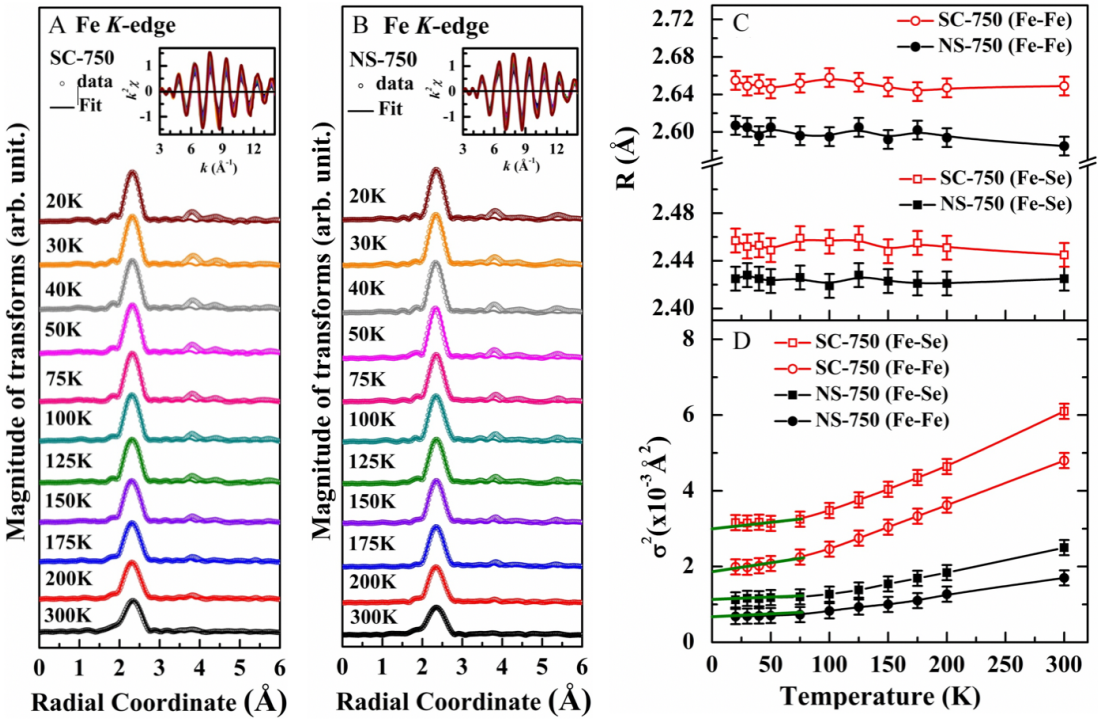
A Fe K-edge
SC-750
data
Fit
B Fe K-edge
NS-750
data
Fit
20K
30K
40K
50K
75K
100K
125K
150K
175K
200K
300K
Magnitude of transforms (arb. unit.)
Radial Coordinate (Å)
C
SC-750 (Fe-Fe)
NS-750 (Fe-Fe)
SC-750 (Fe-Se)
NS-750 (Fe-Se)
R (Å)
D
SC-750 (Fe-Se)
SC-750 (Fe-Fe)
NS-750 (Fe-Se)
NS-750 (Fe-Fe)
σ²(x10⁻³Å²)
Temperature (K)

Figure 5